Detection of convergence areas in Digital Breast Tomosynthesis using a contrario modeling

Article *in* Proceedings of SPIE - The International Society for Optical Engineering · February 2009

DOI: 10.1117/12.807547

4 authors:

Giovanni Palma
IBM
35 PUBLICATIONS **132** CITATIONS
SEE PROFILE

Serge Muller
Institut de Cancérologie Gustave Roussy
213 PUBLICATIONS **1,736** CITATIONS
SEE PROFILE

Isabelle Bloch
Télécom ParisTech
630 PUBLICATIONS **13,973** CITATIONS
SEE PROFILE

Răzvan Iordache
GE Healthcare
79 PUBLICATIONS **361** CITATIONS
SEE PROFILE

Detection of convergence areas in Digital Breast Tomosynthesis using a contrario modeling

G. Palma[a,b], S. Muller[b], I. Bloch[a], R. Iordache[b]
[a] GE Healthcare Europe, 283, rue de la Minière, 78533 Buc, France
[b] TELECOM ParisTech (ENST) - CNRS UMR 5141, 46, rue Barrault, 75013 Paris, France

ABSTRACT

We propose a new method to detect architectural distortions and spiculated masses in digital breast tomosynthesis volumes. To achieve this goal, an a contrario approach is used. In this approach, an event, corresponding to a minimal number of structures converging toward the same location, is defined such that its expectation of occurrence within a random image is very low. Occurrences of this event in real images are then detected and considered as possible lesion locations. During the last step, the number of false positives is reduced through classification using attributes computed on histograms of structure orientations.

The approach was tested using the leave-one-out method on a database composed of 38 breasts (10 containing a lesion and 28 containing no lesion). A sensitivity of 0.8 at 1.68 false positives/breast was achieved.

Keywords: Breast, Digital Breast Tomosynthesis CAD, spiculated masses, a contrario detection

1. INTRODUCTION

Mammography is a widely used technique to diagnose breast cancer. Nonetheless, due to the nature of these images, superimposition of tissues may lead to obscured lesions or false alarms. Digital Breast Tomosynthesis (DBT) is a new 3D imaging technique that potentially overcomes this limitation, but that also increases the amount of data to be reviewed by the radiologist. A CAD system dedicated to this new kind of data may help the radiologist to achieve his detection task, and increase his sensitivity. In DBT datasets, convergence of structures is a common evidence for the presence of malignant lesions (spiculated masses or architectural distortions). In this paper we focus on the detection of such areas using an a contrario approach. First, a naive model is proposed and a convergence measure is computed to detect improbable convergence areas. Secondly, we remove false positives using a classification scheme based on directional gradient features around the potential findings. After detailing these two steps, we will discuss the performance we can get with such an approach on real data.

2. A CONTRARIO MODELING

Because DBT introduces object distortion in the z direction due to the limited angle geometry of the acquisition system, we propose to detect convergence areas independently in the slices of the reconstructed volumes and to use the spatial relationships between the detected areas in successive slices to remove false positives. We first build a statistical model of the structure convergence in slices of normal breasts (naive model). This model involves several random variables for each pixel of a given slice in order to define and retrieve unlikely areas of convergence. These variables correspond to the orientations determined for pixels in a ring-shaped neighborhood centered on the current pixel. Because areas of convergence are usually not present in the naive model, the next step is to find a threshold for unlikely values of these random variables. The a contrario framework is suitable for this purpose and enables to compute such thresholds based on the number of false alarms we accept to generate. To implement this theoretical approach in order to achieve the detection task, we need to extract orientations of structures present in the image and to compute the values of these variables on real DBT slices.

Send correspondence to giovanni.palma@ge.com.

Medical Imaging 2009: Computer-Aided Diagnosis, edited by Nico Karssemeijer, Maryellen L. Giger
Proc. of SPIE Vol. 7260, 72600P · © 2009 SPIE · CCC code: 1605-7422/09/$18 · doi: 10.1117/12.807547

2.1 Random variables and naive model

First a naive model is proposed to express what is to be considered as a regular content of a DBT volume. Thus we consider each slice as an independent and identically distributed field of angles. These angles correspond to the orientation of structures in the image (e.g. the direction orthogonal to the gradient). The main idea is to identify areas of convergence that are unlikely to appear in the naive model, which would correspond to architectural distortions, spiculated masses or fibers.

In order to detect these areas, two random variables are built. They both rely on the construction of two nested circles (of radius r and αr with $\alpha \in]0,1[$ a constant). The smaller circle defines the center of convergence and the ring in between the two circles defines the area where we look for structures converging to this center. This is illustrated in Figure 1(a). The first binary random variable is denoted $K_{c,q,r}$, and is defined as:

$$K_{c,q,r} = \begin{cases} 1 \ \textit{if} \ \tan(\theta)||\overrightarrow{cq}|| \leq \alpha r \\ 0 \ \textit{otherwise.} \end{cases} \tag{1}$$

where θ corresponds to the angle between $\overrightarrow{cq}$ and the orientation at point q.

In the case of a field of angles composed of uniform random variables, we have:

$$P[K_{c,q,r} = 1] = \frac{2}{\pi} \tan^{-1}\left(\frac{\alpha r}{||\overrightarrow{cq}||}\right)$$

We can note that this probability depends on the distance between the point q and the center c as well as the size and ratio of the two circles. Actually, when the two points are getting closer to each other, the probability for this variable to be equal to 1 increases.

We can also note that $K_{c,q,r}$ is not always equal to one when the straight line passing through point q, whose orientation is given by the angle at this point, is intersecting the circle of radius αr, which is centered on point c. This would have been the case if the tangent had been replaced by a sinus in Equation 1. Nonetheless, such a choice would have been a problem since points close to the circle of radius αr may be considered as pointing to the center of convergence when they just intersect the extremity of the disk as illustrated in Figure 1(c). This problem is avoided using the proposed formulation because such points are considered as converging only if they are oriented toward point c.

The second random variable $Z_{c,r}$ is built using the former variables for points q that lie in the subset of the image domain Ω corresponding to the zone between the two circles centered on c and of radius αr and r, respectively, as illustrated in Figure 1(b):

$$Z_{c,r} = \sum_{q \in \Omega / \alpha r < ||\overrightarrow{cq}|| < r} K_{c,q,r} \tag{2}$$

The variable defined in Equation 2 is an indicator of convergence because it represents the number of pixels q that point toward a given center c. It is similar to the measure introduced by Karssemeijer et al.[1] Nonetheless, it is not strictly equivalent to this measure: in our approach, there is no gap between the ring and the small disk used to evaluate the convergence and we also discard points close to this disk that actually do not converge, as explained earlier. Without this last difference, the considered variable would be a special case of what Karssemeijer et al.[1] proposed.

In order to compute the probabilities for this variable to be equal to a given integer, we can use the generating function of $K_{c,q,r}$. More generally, for a random discrete variable X taking values on $\mathbb{Z}^+$, the generating function allows expressing the probabilities to be equal to any integer using a polynomial representation:

$$G_X(x) = \sum_{n=0}^{\infty} P[X = n] x^n$$

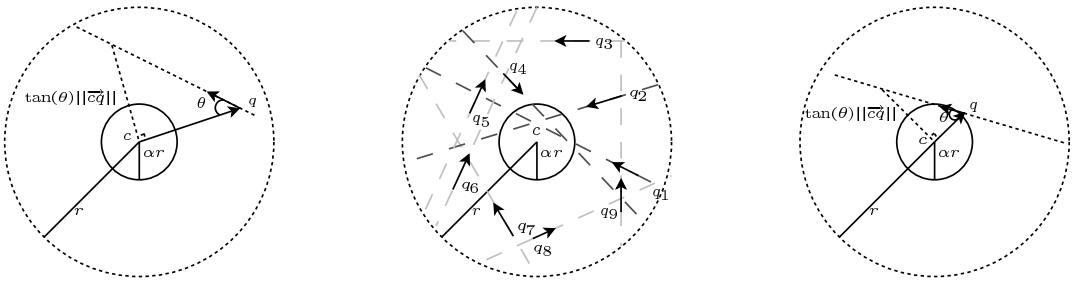

(a) (b) (c)

Figure 1. (a) Nested circles used for the computation of $K_{c,r,q}$ which is here equal to 0. (b) Computation of $Z_{c,r}$: the arrows on the dark dashed lines (passing through q_1, q_2 and q_4) converge while others do not. (c) Example of unintuitive convergence avoided.

In the case of $K_{c,q,r}$, we have for any c, q, r:

$$G_{K_{c,q,r}}(x) = P[K_{c,q,r} = 0] + P[K_{c,q,r} = 1]x$$

Now since we made the assumption that the orientations at different points q are independent, it follows that the different variables $K_{c,q,r}$ are independent. This enables us to compute the generating function of a variable $Z_{c,r}$ by multiplying the $G_{K_{c,q,r}}$ associated to the different points q lying in the ring centered in c defined by the circles of radius αr and r:

$$G_{Z_{c,r}}(x) = \prod_{q \in \Omega / \alpha r < ||\overrightarrow{cq}|| < r} G_{c,q,r}(x)$$

This can be rewritten as:

$$G_{Z_{c,r}}(x) = \prod_{q \in \Omega / \alpha r < ||\overrightarrow{cq}|| < r} (P[K_{c,q,r} = 0] + P[K_{c,q,r} = 1]x) = \sum_{k \in \mathbb{Z}} p_k x^k \tag{3}$$

with $P[Z_{c,r} = k] = p_k$.

The computation of these probabilities is required in order to decide when a value of $Z_{c,r}$ becomes unlikely. The remaining step is to focus on this notion of *unlikely*. Actually, the a contrario framework provides a definition for that using ϵ-meaningful events.

2.2 ϵ-meaningful convergences

The a contrario framework is about detecting events that are unlikely to happen in a naive model. In order to decide whether an event is likely or not, we can use the definition of ϵ-meaningful events provided by Desolneux et al.[2]

DEFINITION 2.1. *An event is ϵ-meaningful if the expectation of the number of its occurrences in the image is less than ϵ.*

This definition introduces a new parameter ϵ that corresponds to our acceptance of unlikely events. If we can make their detections depend on this parameter and if our naive model holds for real data, then this will be an intuitive way to tune the performance of our detection since it actually corresponds the number of false positives we agree to accept in the naive model.

Back to the random variables we previously introduced, and more specifically to $Z_{c,r}$, we can define an event that corresponds to the detection of convergence areas. To do so we can decide that c is the center of such a zone

defined by the radius r if $Z_{c,r} \geq \lambda$ with λ a threshold. Obviously, the probability of occurrence of this event for a given pair (c, r) will depend on the value of this threshold.

THEOREM 2.1. *The event $Z_{c,r} \geq \lambda_r$ is ϵ-meaningful with λ_r defined as:*

$$\lambda_r = \min\left\{\lambda \in \mathbb{N} / P[Z_{c,r} \geq \lambda] \leq \frac{\epsilon}{M}\right\} \tag{4}$$

where M is the total number of couples (c, r) to be considered within the image (values of r range between $r_{\min}$ and $r_{\max}$).

Proof. The expectation of the number of convergence areas detections is:

$$E_Z = \sum_{r \in [[r_{\min}, r_{\max}]]} \sum_{c \in \Omega} P[Z_{c,r} \geq \lambda_r]$$

Now using Equation 4, we have:

$$\sum_{r \in [[r_{\min}, r_{\max}]]} \sum_{c \in \Omega} P[Z_{c,r} \geq \lambda_r] \leq \sum_{r \in [[r_{\min}, r_{\max}]]} \sum_{c \in \Omega} \frac{\epsilon}{M}$$

Furthermore, since M corresponds to the number of considered couple (c, r) in an image, we get:

$$\sum_{r \in [[r_{min}, r_{\max}]]} \sum_{c \in \Omega} \frac{\epsilon}{M} = M \frac{\epsilon}{M} = \epsilon$$

Thus, we have $E_Z \leq \epsilon$. For this reason Theorem 2.1 is verified. □

Let us finally remark that the choice of λ_r depends on the radius r. This is because when the radius becomes larger, the number of points q to check increases, leading to a potentially higher value of Z. On the other hand, the position of c in the image does not impact the threshold value.

2.3 Detection of ϵ-meaningful convergences

In order to detect convergence areas, the variables $Z_{c,r}$ are computed for all $c \in \Omega$ and $r \in [[r_{\min}, r_{\max}]]$. The decision is then made using the thresholds proposed in Theorem 2.1. In order to compute these thresholds, for each radius r, the probabilities $P[K_{c,q,r} = 1]$ for the q lying in the ring are computed in order to use Equation 3, which is required to use Equation 4. Since the probabilities associated to $K_{c,q,r}$ do not depend on the location of c but rather on the distance $||\overrightarrow{cq}||$, this can be done one time for an arbitrary center location.

The angle map to be used for this step is derived from the directions orthogonal to gradients in the input image. Note that these gradients should not be computed using usual linear filtering approaches (Gaussian derivatives, Sobel, etc.) because it would break the independence assumption made during the computation of thresholds. This may be not intuitive, but if we use such approaches, statistics of $Z_{c,r}$ will be modified invalidating our approach to compute the thresholds unless we consider an orientation map of correlated random variables. In that case, the correlation would depend on the convolution step used during the computation of the gradient map. In our implementation, we used blocks of four (2×2) pixels that do not overlap (see Figures 2(a) and 2(b)). For each block, gradients are computed using the differences of mean of pixels along the x and y directions as illustrated in Figures 2(c) and 2(d). This results in a gradient vector for each block of four pixels, thus the gradient map is sub-sampled in comparison to the original image. This sub-sampling allows having a more robust estimation of the gradient map. If we use larger blocks, the sub-sampling will be more important resulting in a smoother gradient map at the expense of degrading the resolution. While this may be dramatic for small lesions, it may be useful for larger ones. In order to combine the benefits from different block sizes, we can use a multi-scale approach by doubling the width of the blocks at each step and by reducing the value of $r_{\max}$ accordingly. This approach also speeds up the computation time.

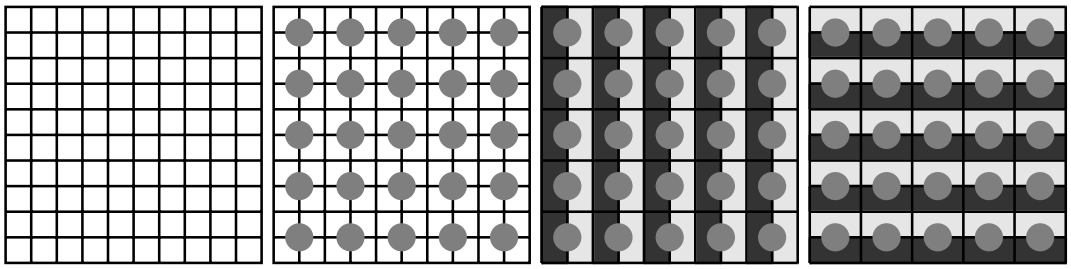

(a) (b) (c) (d)

Figure 2. Extraction of an orientation map using a non correlated gradient map. (a) Original image where the pixels are represented by white squares. (b) Blocks of four pixels that do not overlap and that are used for the gradient map computation. Gray disks represent the location of the gradient vectors. (c) Gradient computation in the x direction. (d) Gradient computation in the y direction.

3. FALSE POSITIVES REDUCTION

Spiculated lesions and architectural distortions are not the only structures that may be described using a convergence pattern in DBT datasets. Sometimes, fibers or other structures can also be caught by the former a contrario approach. In order to discard them, for each slice, the ϵ-meaningful events are grouped, and then classified. Finally the remaining suspicious areas are associated in 3D.

3.1 Aggregation of the ϵ-meaningful events

Because a convergence area is usually not detected for a single center c and a single radius r, some of the meaningful events retrieved from the first detection stage can be associated together. This step will simplify the further false positives reduction process. This aggregation step is simply done by computing a map A as follows:

$$A = \bigcup_{(c,r)/Z_{c,r} \geq \lambda_r} D_{c,\alpha r} \tag{5}$$

with $D_{c,r}$ the disk of radius r centered at point c. Eventually, a connected component labeling for each slice enables to extract findings in order to decide if they are true or false positives.

3.2 Feature selection

To reduce the amount of false positives, we implemented several measures (entropy, variance, skewness, kurtosis, etc.) on histograms built from structure orientations in regions detected in the first stage. As opposed to the detection step of ϵ-meaningful convergences, the orientations were obtained using Gaussian second derivative[1,3] in order to be more robust to noise. Because of the amount of data available for tests, these values were not combined together using classical classifiers (the feature space would have been too sparse to produce relevant results). Only the best feature, which is the entropy of structure orientations, was kept. Its computation relies on the zone $\tilde{A}_i$ which depends on the considered connected component A_i of A:

$$\tilde{A}_i = \bigcup_{(c,r)/(c \in A_i) \wedge (Z_{c,r} \geq \lambda_r)} D_{c,r} \tag{6}$$

$\tilde{A}_i$ is then used to build a histogram of angles corresponding to the orientation at all points $p \in \tilde{A}_i$. Elements of this histogram are also weighted by the magnitude of the orientation map. Then the actual feature corresponds to the entropy of this histogram. This process is illustrated in Figure 3.

This process allows extracting the main orientations of structures that are present in $\tilde{A}_i$. Thus, we can expect that a crossing fiber will produce a peaked histogram, while a spiculated lesion will have a more homogeneous repartition of orientations. With such an interpretation, it makes sense to use the entropy of the histogram to distinguish the two cases.

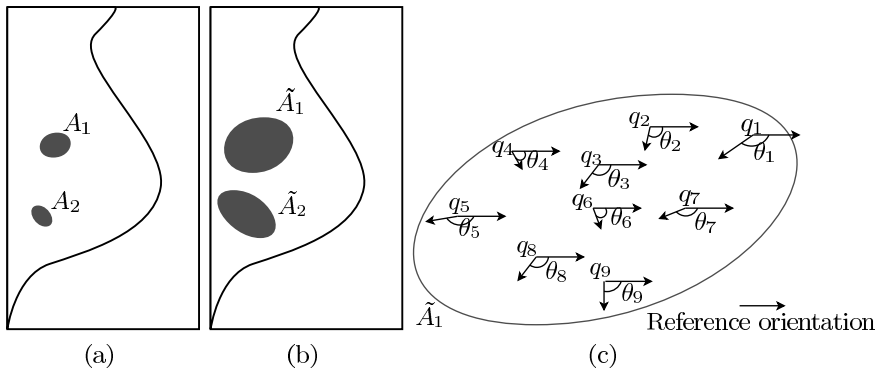

Figure 3. (a) Illustration of Equation 5. Aggregation A of the a contrario detection result: two connected components A_1 and A_2 are present in the breast. (b) Illustration of Equation 6: areas $\tilde{A}_1$ and $\tilde{A}_2$ used to compute histogram features in order to decide whether the former findings are actual lesions. (c) Illustration of structure orientations represented by the angles θ_k used to build these histograms for a given $\tilde{A}_i$.

Thresholds were computed from learning databases composed of areas marked as suspicious in the first stage and that were actual biopsy-proven lesions. This learning database was composed from the independent processing of slices, which means that a lesion appearing on several slices would generate several components. Thresholds were deduced using a parameter n corresponding to the number of false negatives allowed on learning data. For this reason, n was not corresponding to the sensitivity of the overall method, but rather to an intuitive way to tune it.

3.3 3D aggregation

In order to use the 3D information, the connected components of a 3D set composed of the sets A associated to the different slices of the volume are labeled. Then, each component is kept if the classification step tagged the finding as lesion in at least one slice. Thus we expect to make the decision based on the slice where the lesion is the most obvious. Moreover, keeping the whole connected component, as defined before the classification, avoids to split a lesion when it is misclassified in some intermediate slices.

4. RESULTS

4.1 Database

The proposed CAD scheme was evaluated on a set of 38 breasts reconstructed using the SART algorithm.[4] These data were reviewed by experienced radiologists and ten breasts were containing a spiculated lesion or an architectural distortion, while the remaining ones were healthy. Ground truth for the actual malignity of the lesions was obtained by histology.

4.2 Illustration

Figures 4 illustrates the whole detection chain on a given slice (Figure 4(a)). Figure 4(b) presents the result of the aggregation (inner part of the rings) of several meaningful events. The two findings resulting of the aggregation are considered in the next step intended to reduce the number of false positives. Using the entropy of structure orientations, the false positive can be removed while the actual lesion is preserved, as shown in Figure 4(c).

The histograms corresponding to the lesion and the false positive are presented in Figure 5(b) and 5(a), respectively. The main difference that can be seen on these plots is that the false positive has only two privileged directions on its histogram, one around -0.1 and another one around $\pm\frac{\pi}{2}$, while for the actual lesion no priviledged orientation is observed. In this particular example, the histograms fit what we would expect according to the data: the false positive is due to the crossing of two fibers and spicules of the lesion are coming from every direction. The validation step tends to verify this assumption on the whole database.

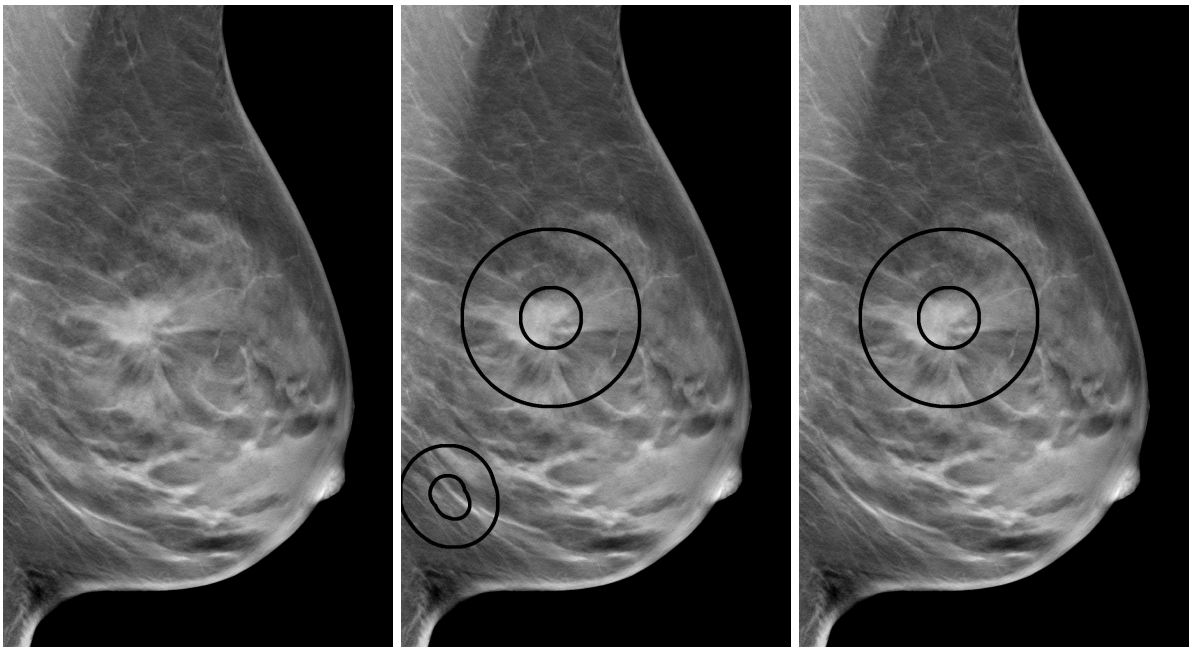

(a) (b) (c)

Figure 4. (a) A slice of a DBT volume containing a lesion. (b) Result of the a contrario detection. (c) Result after false positives reduction.

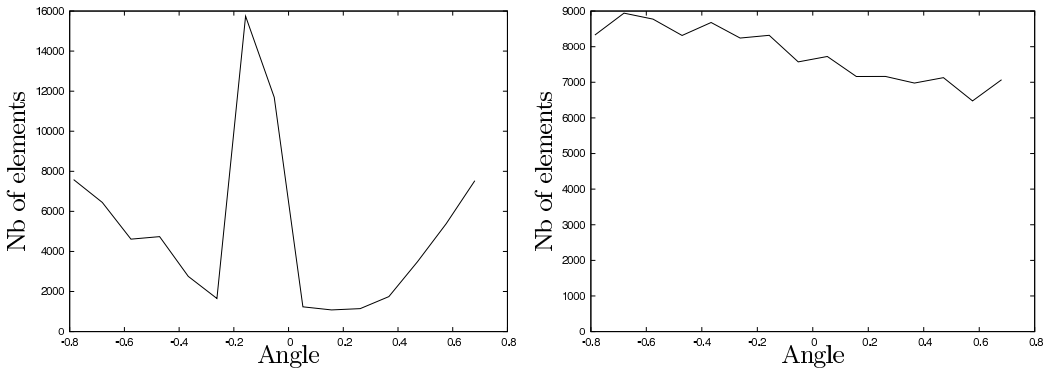

(a) (b)

Figure 5. Example of angle histograms for the false positive (a) and the actual lesion (b) presented in Figures 4(b).

4.3 Performance

The evaluation was done using the leave-one-out method for various values of parameter n, using the entropy of the histograms of structure directions during the false positives (FPs) reduction step. These different n values led to the Free-Response Receiver Operating Characteristic (FROC) curve shown in Figure 6. The number of FPs was evaluated on 28 breasts containing no cancer. A sensitivity of 0.8 with a FPs rate of 1.68 per case or a sensitivity of 1 with 2.5 FPs per case was obtained. Even if these results are not completely reliable because of the relatively small database size, they tend to validate the approach. Furthermore they are comparable with existing approaches.[5–8] Note that the false positive rate is not much improved when the sensitivity is getting worst, which is not really an issue since a CAD system has to perform at a high sensitivity rate. Nonetheless, because of the database size, we cannot be conclusive on this behavior and on the actual performance of the approach. Again, this experimentation only tends to prove that the approach should work on real data.

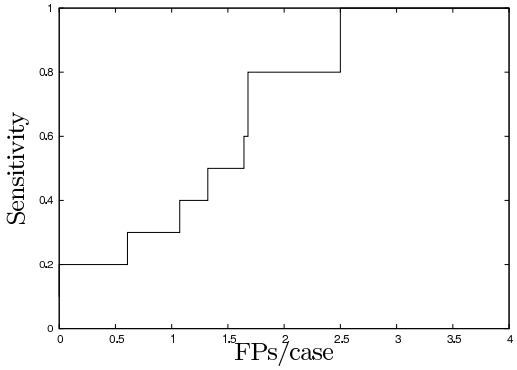

Figure 6. FROC curve of the overall processing chain.

5. CONCLUSIONS

We have proposed a method to detect architectural distortions and spiculated lesions in DBT volumes. This approach is based on an a contrario framework originally designed to detect alignments of points in an image[2] and applied to the modeling of the human detection task in complex background images.[9] It relies on the definition of what should be a regular content of an image in order to detect patterns that are unlikely to appear. In our case we modeled the slices of DBT volumes as random orientation maps in order to derive their probabilities of convergence. Using the definition of ϵ-meaningful events[2] we proposed an easy way to tune the threshold to be used for the measure of convergence.[1] Finally, because lesions are not the only source of convergence, we proposed to reduce false positives using a feature based on the entropy of orientation histograms computed in the areas where potential lesions stand.

Using this final false positives reduction step, the CAD scheme was tested on 38 breasts (10 containing a biopsy-proven lesion and 28 containing no lesion) achieving high sensitivity at a reasonable false positives rate. Even if the database is not large enough to actually conclude on the real performances of the approach, it tends to demonstrate its validity.

The next key step will be to increase the database size. This will enable to use a better classification step and to be more conclusive on both sensitivity and specificity of the approach.

REFERENCES

[1] Karssemeijer, N. and te Brake, G. M., "Detection of stellate distortions in mammograms," *IEEE Transactions on Medical Imaging* 5(5), 611–619, (1996).
[2] Desolneux, A., Moisan, L., and Morel, J., "Meaningful alignments," *International Journal of Computer Vision* 40(1), 7–23, (2000).
[3] Koenderink, J. J. and van Doorn, A. J., "Generic neighborhood operators," *IEEE Trans. Pattern Anal. Mach. Intell.* 14(6), 597–605, (1992).
[4] Andersen, A. H. and Kak, A. C., "Simultaneous algebraic reconstruction technique (SART): A superior implementation of the ART algorithm," *Ultrasonic Imaging* 6(1), 81–94, (1984).
[5] Cheng, H. D., Shi, X. J., Min, R., Hu, L. M., Cai, X. P., and Du, H. N., "Approaches for automated detection and classification of masses in mammograms," *Pattern Recogn.* 39(4), 646–668, (2006).
[6] Chan, H., Wei, J., Sahiner, B., Rafferty, E. A., Wu, T., Roubidoux, M. A., Moore, R. H., Kopans, D. B., Hadjiiski, L. M., and Helvie, M. A., "Computer-aided Detection System for Breast Masses on Digital Tomosynthesis Mammograms: Preliminary Experience," *Radiology* 237(3), 1075–1080, (2005).
[7] Chan, H.-P., Wei, J., Zhang, Y., Helvie, M. A., Moore, R. H., Sahiner, B., Hadjiiski, L., and Kopans, D. B., "Computer-aided detection of masses in digital tomosynthesis mammography: Comparison of three approaches," *Medical Physics* 35(9), 4087–4095, (2008).
[8] Singh, S., Tourassi, G. D., Baker, J. A., Samei, E., and Lo, J. Y., "Automated breast mass detection in 3D reconstructed tomosynthesis volumes: A featureless approach," *Medical Physics* 35(8), 3626–3636, (2008).
[9] Grosjean, B., Muller, S., and Souchay, H., "Lesion detection using an a-contrario detector in simulated digital mammograms," *Medical Imaging 2006: Image Perception, Observer Performance, and Technology Assessment* 6146(1), 61460S, SPIE, (2006).